Cell Communication and Signaling

BRIEF REPORT Open Access

DHODH links mitochondrial bioenergetics, one-carbon metabolism, and DNA repair to sustain aggressive prostate adenocarcinoma

Saiswaroop Rajaratnam[1], Danthasinghe Waduge Badrajee Piyarathna[1], Ranjit K. Mehta[2], Venugopalareddy Mekala[3], Jun Hyoung Park[4], Uttam Rasaily[1], Vani Venkatappa[1], Karthik Reddy Kami Reddy[1], Vasanta Putluri[5], Kaveri Goel[6], Sandra L Grimm[1], Sai Manohar Thota[1], Taylor Morrison[6], Cristian Coarfa[1,9], Benny Abraham Kaipparettu[4,9], Chao Cheng[3], Nagireddy Putluri[1,5,9], Jeffrey A Jones[7,8,9], Mukesh K. Nyati[2], Michael Ittmann[10], Natalie R Gassman[6] and Arun Sreekumar[1,9*]

Abstract

Background Dihydroorotate dehydrogenase (DHODH) is a mitochondrial enzyme that connects de novo pyrimidine biosynthesis with the electron transport chain (ETC) function. However, its broader role in prostate cancer (PCa) signaling and response to therapy remains unclear.

Methods We combined transcriptomic, metabolomic, epigenomic, and functional analyses with clinical outcome data to explore the effects of DHODH depletion in ancestry-annotated European American (EA) and African American (AA) prostate cancer cell line models.

Results DHODH was markedly overexpressed in malignant prostate epithelial cells and was abundant in tumors. Its knockdown hindered cell proliferation by causing pyrimidine depletion, while unexpectedly increasing oxidative phosphorylation, ETC complex activity through metabolic stress–driven mitochondrial biogenesis. This also led to oxidative stress due to an imbalance in $NADP^+$/NADPH. Metabolomics indicated enhanced one-carbon metabolism and increased overall DNA methylation. Whole-genome bisulfite sequencing of DHODH KD cells identified regions with differential methylation in genes related to epithelial–mesenchymal transition (EMT) and inflammatory signaling. Functionally, the loss of DHODH decreased cell migration and metastasis and downregulated genes involved in nucleotide excision repair, mismatch repair, and base excision repair.
Additionally, it upregulated a subset of Y-family DNA polymerases, which facilitate error-prone lesion bypass. This was associated with more unrepaired DNA damage and, paradoxically, higher clonogenic survival under genotoxic stress. Clinically, low DHODH expression was linked to shorter biochemical recurrence–free survival after radiotherapy combined with androgen deprivation therapy.

*Correspondence:
Arun Sreekumar
Arun.Sreekumar@bcm.edu

Full list of author information is available at the end of the article

Conclusions DHODH functions as a crucial regulator of metabolism, epigenetics, and genomics in prostate cancer, coordinating mitochondrial respiration, one-carbon metabolism, and DNA repair signaling to promote tumor growth and improve treatment outcomes. Its absence introduces vulnerabilities in genome stability, supporting the idea of combining DHODH inhibitors with DNA repair–targeted therapies for the treatment of prostate cancer.

Keywords DHODH, Prostate adenocarcinoma, Mitochondria, Methylation, DNA repair

Introduction

Prostate cancer (PCa) is the most common non-skin malignancy in men worldwide. It is marked by significant racial disparities, with African American (AA) men experiencing both a higher incidence and more than twice the mortality rate of European American (EA) men [1, 2]. While socioeconomic factors and access-to-care issues contribute to these differences, increasing evidence suggests that inherent molecular and metabolic differences drive the aggressive clinical behavior seen in AA prostate tumors [3–8]. Understanding these tumor-intrinsic factors is crucial for developing targeted interventions to reduce this survival gap [9].

One emerging hallmark of aggressive PCa is dysregulated nucleotide metabolism, which promotes unchecked cell growth and damages genomic stability. Recent studies, including those from our lab, have shown increased uracil misincorporation and higher levels of pyrimidine base damage in clinical samples from AA patients, suggesting that abnormal de novo pyrimidine biosynthesis and faulty DNA repair contribute to tumor development [4, 10]. However, the specific metabolic enzymes involved in these disruptions and their role in PCa have not been thoroughly examined.

Dihydroorotate dehydrogenase (DHODH) plays a key role in nucleotide metabolism as the rate-limiting mitochondrial enzyme involved in de novo pyrimidine synthesis. It catalyzes the oxidation of dihydroorotate to orotate and transfers electrons to the respiratory chain [11]. In addition to its traditional function in nucleotide production, DHODH is linked to broader mitochondrial activities—regulating redox balance, supporting one-carbon metabolism, and modulating epigenetic landscapes by regulating S-adenosylmethionine pools [12, 13]. Increased DHODH levels have been observed in various cancers, where it helps meet biosynthetic needs and enhances cell survival under metabolic stress [14]. High DHODH expression leads to increased cell proliferation and impacts Androgen synthesis in prostate cells [15].

Using combined transcriptomics, methylation sequencing, and metabolomics analyses, along with genetic disruption of DHODH in various ancestry-defined PCa cell line models, we demonstrate that DHODH regulates mitochondrial bioenergetics, folate-based one-carbon metabolism, DNA methylation capacity, and the accuracy of base excision repair. Functional assays demonstrate that DHODH promotes tumor cell proliferation, migration, and metastasis in vivo, with AA-derived models exhibiting a heightened dependence on DHODH activity. These results establish DHODH as a key regulator of metabolism, the epigenome, and genomic stability in PCa, positioning it as a potential therapeutic target whose inhibition might effectively counteract aggressive disease. Furthermore, combining DHODH inhibitors with standard-of-care regimens may potentiate therapeutic efficacy in patients with PCa.

Materials and methods

The cancer genome atlas (TCGA) and bulk RNA dataset analysis

TCGA Gene expression data acquisition and preprocessing for prostate adenocarcinoma (PRAD) samples and their clinical information were obtained from the Broad Institute's Firebrowse (http://firebrowse.org) [16]. A total of 546 patient sample TPM values were obtained and transformed to log2(TPM + 1) to stabilize variance across the dynamic range. The associated clinical metadata included 494 tumor samples and 52 normal prostate tissue samples. Additional clinical variables, such as race (African American and European American), were also included in this study for comparative analysis.

In addition to the TCGA-PRAD dataset, gene expression profiles were also obtained from the Gene Expression Omnibus (GEO), specifically from the GSE70768 dataset, which includes both tumor and normal prostate tissue samples [17]. This dataset also provides detailed clinical information, including tumor cellularity percentages for each patient. To enhance the analysis of tumor composition and its relationship with gene expression, tumor percentage data were incorporated from the GSE70768, GSE17951 [18], and GSE8218 [19] datasets. GSE116918 was used to study the effect of radiation therapy on the DHODH expression in Prostate Cancer patients [20]. Code for reproducing and analyzing bulk RNA-seq data is available on GitHub: https://github.com/venu887/DHODH_Prostate_Cancer. We used the Wilcoxon test to compare the two groups and assess statistical significance in the dataset, and the Pearson correlation test to evaluate the strength and significance (p-value < 0.05) of correlations between variables.

Single cell RNA-sequencing (scRNAseq) transcriptomic analysis

Raw single-cell RNA sequencing data for the GSE141445 dataset were downloaded from the Gene Expression Omnibus (GEO) [21]. The raw count matrix was imported into R and organized with genes as rows and cell barcodes as columns. A Seurat object was created after applying initial quality filters: genes expressed in fewer than three cells ("min.cells" = 3) were excluded, and cells with fewer than fifty detected genes ("min.features" = 50) were removed. Cell barcode suffixes were parsed to assign sample identities, which were stored as metadata for downstream integration.

Quality control was performed to ensure that only high-quality cells were retained. The percentage of mitochondrial transcripts per cell was calculated using the pattern "MT". Cells with fewer than fifty detected genes or more than 5% mitochondrial gene expression ("percent.mt" > 5) were discarded, as such profiles are associated with low-quality or dying cells. Each sample was normalized independently, and variable features were identified with the variance-stabilizing transformation method ("selection.method" = "vst"), keeping the top 2,000 most variable genes ("nfeatures" = 2000) per sample. To correct for inter-sample variation, Seurat's anchor-based integration workflow was applied. Integration anchors were identified across samples using canonical correlation analysis (CCA), with the top 100 dimensions ("dims" = 1:100) used to capture shared sources of variation. Integration was then performed with "IntegrateData()", generating a batch-corrected expression matrix. The integrated Seurat object was saved to preserve reproducibility.

The integrated dataset was scaled and subjected to dimensionality reduction. Principal component analysis (PCA) was first performed, and the first 30 Principal Components (PCs, "dims" = 1:30) were used to construct a shared nearest-neighbor graph. Clustering was carried out using Seurat's graph-based method at a resolution of 0.8. For visualization, two nonlinear embeddings were computed: Uniform Manifold Approximation and Projection (UMAP) using the first 30 PCs, and t-distributed Stochastic Neighbor Embedding (t-SNE) using the first 20 PCs. Cluster-specific marker genes were identified using the Wilcoxon rank-sum test, restricted to positive markers only ("only.pos" = TRUE). Genes were considered markers if they were expressed in at least 25% of cells within a cluster ("min.pct" = 0.25) and showed a log fold change greater than one ("logfc.threshold" = 1). Marker gene sets were compared against curated prostate cancer–related reference signatures from CellMarkerDB (http://www.bio-bigdata.center) and published datasets.

Cluster annotation was performed through a combination of enrichment analysis and manual curation. Enrichment scores quantified the overlap between cluster markers and curated signatures, with Fisher's exact test used to assess enrichment significance. When database matches were ambiguous, canonical lineage markers were inspected to refine assignments. Final cluster identities included epithelial cells, T cells, B cells, plasma cells, NK cells, dendritic cells, monocytes, macrophages, mast cells, fibroblasts, endothelial cells, pericytes, and tumor cells.

Expression of marker genes across clusters was visualized using dot plots, which show both the percentage of cells expressing a gene and the corresponding expression level. For targeted analysis of DHODH, normalized expression values were extracted from the RNA assay of the integrated object. To ensure robust inference, only cell types containing at least twenty DHODH-positive cells were retained. Expression distributions were displayed with violin plots, and pairwise Wilcoxon rank-sum tests were conducted, comparing each cell type against epithelial cells as the reference population.

All intermediate objects, including the integrated Seurat object, cluster marker lists, annotation tables, and visualization outputs, were saved to maintain reproducibility. By combining stringent quality control, CCA-based integration, clustering, and marker-guided annotation, this pipeline enabled systematic dissection of the cellular composition of GSE141445. It facilitated the investigation of DHODH expression across the prostate tumor microenvironment. Code for reproducing and analyzing scRNAseq data is available from GitHub:
https://github.com/venu887/DHODH_Prostate_Cancer.

Cell culture

22RV1 and MDA-PCa-2b were used for the study. The MDA-PCa-2b cell line was generously provided by Dr. Nora Navone (MD Anderson Cancer Center), and the 22RV1 cell line was purchased from ATCC (CRL-2505). Short Tandem Repeat (STR) profiling was performed on all cell lines at the MD Anderson Cytogenetics and Cell Authentication Core to confirm their authenticity. Routine mycoplasma testing was conducted using the MycoAlert™ detection kit (Lonza, Anaheim, CA) to ensure the cultures remained free of contamination. In our study, we used the MDA-PCa-2b and 22RV1 cell lines as representative models for African American (AA) and European American (EA) PCa, respectively. These cell lines have been ancestry-verified in our lab and by others [22, 23]. Both cell lines were derived from metastatic PCa patients, allowing us to examine the functional consequences of DHODH KD. These cell lines were maintained as per standard procedures [8].

Lenti-viral transduction

Lentiviral vectors carrying shRNA constructs targeting DHODH or non-targeting control shRNA were

purchased from Horizon Discovery, Cambridge, UK (VSC11709, V3SVHS02_5824977, V3SVHS02_6798774). Lentiviral constructs for DHODH overexpression were purchased from Genecopia (Cat No: I1526). The virus was harvested in low-passage 293T cells. For lentiviral transfection, plasmid DNA was complexed using Lipofectamine 2000 (Thermo Fisher Scientific) according to the manufacturer's protocol. For infection, target cells were seeded in 24-well plates at approximately 50% confluence and incubated overnight. The following day, cells were transduced with 1 mL of filtered viral supernatant mixed with 1 mL of complete medium. Polybrene (Sigma-Aldrich TR-1003) was added to a final concentration of 5–6 µg/mL to enhance transduction efficiency. Following transduction, knockdown cells were selected with Puromycin (Gibco™ Puromycin), and overexpression was selected with Geneticin (Geneticin™ G418 Sulfate). Transduction efficiency was confirmed by fluorescence microscopy, with Green Fluorescent Protein (GFP) expression indicating knockdown expression and Red Fluorescent Protein (RFP) indicating overexpression.

Quantitative real-time polymerase chain reaction

Total RNA was extracted from cultured cells using the Aurum™ Total RNA Mini Kit (Bio-Rad) following the manufacturer's protocol. RNA concentration, purity (A260/A280 ratio), and cDNA conversion were performed as per previously described methods [8]. Quantitative real-time PCR (RT-qPCR) was performed using SYBR™ Green PCR Master Mix (Life Technologies, Cat# 4385614) on a real-time thermal cycler. Expression levels were normalized to housekeeping genes, depending on the experimental context. Primer sequences used in this study are provided below (Table 1).

Protein extraction, estimation, and Western blot

Protein extraction, estimation, and western blot were performed as per previously established methods [8]. Briefly, Cell pellets were thawed on ice and lysed in 100–200 µL of RIPA buffer (Thermo Fisher Scientific) supplemented with protease and phosphatase inhibitors (1 µL per 100 µL buffer). Lysates were incubated on ice for 10 min, sonicated for 30 s, cooled for an additional 5 min, and centrifuged at 14,500 rpm for 10 min at 4 °C. The supernatant was collected and stored on ice or at – 80 °C. Protein concentration was determined using the Pierce™ BCA Protein Assay Kit (Thermo Fisher Scientific) according to the manufacturer's instructions. Samples (30 µg) were separated on 4–15% Mini-PROTEAN Tris-Glycine gels (Bio-Rad, Cat# 4561086) at 100 V for ~ 1.5 h. Proteins were transferred to PVDF membranes (Immobilon-P, 0.45 µm; Merck Millipore) using a wet transfer system at 12 V for 1.5 h. Membranes were blocked with 5% BSA in TBST for 1 h at room temperature and incubated overnight at 4 °C with primary antibodies against DHODH (Proteintech, Cat# 14877-1-AP) diluted 1:1000 in 5% BSA/TBST. After washing, membranes were incubated with HRP-conjugated secondary antibodies (1:3000) for 1 h at room temperature. Signal detection was performed using a chemiluminescent substrate (Thermo Fisher Scientific, Cat# 34579) and imaged with the Chemi-Doc System (Bio-Rad). GAPDH (Cell Signaling Technology, Cat# 2118) was used as a loading control. The blots were normalized with GAPDH and quantified using Sciugo (https://sciugo.com).

Table 1 Table representing primer sequences used for the study

Gene	Primer Sequence
DHODH - Forward	5′-GGAGACACCTGAAAAAGCGG-3′
DHODH - Reverse	5′-CAGAGTCGGCATCAGGTGTT-3′
TET1 - Forward	5′-CATCAGTCAAGACTTTAAGCCCT-3′
TET1 - Reverse	5′-CGGGTGGTTTAGGTTCTGTTT-3′
TET2 - Forward	5′-GATAGAACCAACCATGTTGAGGG-3′
TET2 - Reverse	5′-TGGAGCTTTGTAGCCAGAGGT-3′
MITOCHONDRIAL DNA - Forward	5′-GTCAACCTCGCTTCCCCACCCT-3′
MITOCHONDRIAL DNA - Reverse	5′-TCCTGCGAATAGGCTTCCGGCT-3′

Treatment studies

Treatment studies were carried out by treating cell-lines with optimal concentrations of reagents (Sigma U3003-5G). Briefly, cells were treated with 100µM uridine. The treatment time was titrated based on the experimental needs. After the stipulated time, cells were harvested and used for experiments.

BrDU growth assay

Cell proliferation was assessed using a BrdU (5-bromo-2'-deoxyuridine) incorporation assay, following the manufacturer's protocol. Briefly, 5,000–20,000 cells were seeded into each well of a 96-well plate and incubated for 24 h at 37 °C. BrdU labelling reagent was then added, and cells were incubated for 24 h to allow incorporation into newly synthesized DNA. Following incubation, cells were fixed, washed, and incubated with a horseradish peroxidase (HRP)-conjugated anti-mouse IgG secondary antibody. Subsequently, peroxidase substrate was added to each well, and absorbance was measured at 450 nm using a microplate reader. Data were analyzed and visualized using GraphPad Prism software (version 10.4.2).

RNA sequencing and analysis

The cell pellets were washed with Phosphate Buffer Saline. Three million cells were harvested and counted per replicate. RNA extraction was performed using the Aurum™ Total RNA Mini Kit (Bio-Rad). Libraries were prepared using the ABclonal mRNA-seq Library Prep Kit for Illumina (poly (A) selection). RNA integrity and quantification were confirmed on the AATI Fragment

Analyzer and quantitative PCR. Novogene Corporation in Sacramento performed quality assessment and sequencing. Sequencing was performed using Illumina NovaSeq X Plus (PE150). Raw RNA-seq reads were first processed for adapter and quality trimming using Trim Galore (v0.6.7) with default parameters. Trimmed reads were then aligned to the human reference genome (GRCh38/hg38) using HISAT2 (v2.2.1) with default settings and the corresponding HISAT2 index built from the Ensembl GRCh38 primary assembly. Aligned reads were sorted and converted to BAM format using SAMtools (v1.11). Gene-level read quantification was performed using featureCounts from the Subread package (v2.0.1), with annotation based on the Ensembl GRCh38 GTF file. Only uniquely mapped reads were counted, and strand-specific counting was applied as appropriate for the library type. Differential gene expression analysis was conducted using DESeq2 (v1.38.3) in R. Raw count data were imported, and lowly expressed genes were filtered out. Counts were normalized using DESeq2's median-of-ratios method. Differentially expressed genes (DEGs) were identified based on an adjusted p-value (FDR) threshold of 0.05 and a log2 fold change ± 1.

Biochemical characterization of mitochondria

Electron transport chain (ETC) enzyme activities were measured in triplicate using the Tecan Infinite M200 microplate reader, following established protocols [24, 25]. Activities of individual ETC complexes and citrate synthase were normalized to total protein concentration. Enzymatic activity rates were determined by calculating the slope of the linear portion of the reaction curve. To account for mitochondrial content, ETC complex activities were further normalized to citrate synthase activity. Data visualization and statistical analysis were performed using GraphPad Prism version 10.4.2. Statistical significance was assessed using an unpaired two-tailed t-test.

Seahorse XF mito stress assay

Mitochondrial respiration was evaluated using the Seahorse XF Analyzer (Agilent Technologies) according to the manufacturer's protocol. Briefly, 10,000–15,000 cells were seeded in 100 µL of complete growth medium per well in an XF Cell Culture Microplate and incubated for 24 h at 37 °C. The sensor cartridge was hydrated overnight in XF Calibrant at 37 °C in a non-CO_2 incubator. On the day of the assay, cells were washed and equilibrated with Seahorse assay medium (XF Base Medium supplemented with 1 mM sodium pyruvate, 2 mM glutamine, and 10 mM glucose) and incubated for 45–60 min at 37 °C in a non-CO_2 incubator. Oligomycin (1 µM), FCCP (1 µM), and rotenone/antimycin A (0.5 µM) were prepared in assay medium and loaded into Ports A, B, and C, respectively. Following calibration, the assay was performed according to standard procedures. Data was normalized with protein absorbance in Wave 2.6.0. Furthermore, they were analyzed using Wave software (Agilent Technologies) and visualized using GraphPad Prism (version 10.4.2).

Reactive oxygen species (ROS) detection using ROS-Glo™ assay (Promega)

Cells were seeded at the desired density in a volume of ≤ 80 µL per well into 96-well white opaque plates or white-walled plates with clear bottoms and were incubated at 37 °C in a humidified CO_2 incubator for 24 h. Following incubation, 125 µM hydrogen peroxide (H_2O_2) was added to each well, and the plates were returned to the incubator for an additional 6 h. After H_2O_2 treatment, 100 µL of freshly prepared ROS-Glo™ Detection Solution (Promega) was added to each well. Plates were then incubated as per the manufacturer's recommendations, and luminescence was measured using a plate reader and visualized using GraphPad Prism software (GraphPad Prism version 10.4.2).

NAD^+/NADH-Glo™ and $NADP^+$/NADPH-Glo™ assay (Promega)

Intracellular NAD^+/NADH and $NADP^+$/NADPH levels were measured using the Glo™ Assay kit (Promega) according to the manufacturer's protocol. Briefly, cells were seeded in white opaque 96-well plates and incubated at 37 °C in a humidified CO_2 incubator. Detection Reagent (Promega) was added to each well. Plates were gently and briefly shaken to ensure proper mixing and cell lysis. The plates were then incubated at room temperature for 30–60 min to allow the luminescent signal to develop. Luminescence was measured using a plate reader, and data were analyzed using GraphPad Prism software (version 10.4.2).

Targeted mass spectrometry (LC-MS-triple quad)

Three million cells per replicate ($n = 3$) were harvested and subjected to three freeze–thaw cycles in liquid nitrogen for complete lysis. After adding 750 µL ice-cold extraction buffer [(4:1) Methanol water], samples were sonicated for 30 s on ice. Chilled chloroform (450 µL) and LC/MS-grade water (150 µL) were added, followed by vortexing and 5 min sonication on ice. Samples were incubated at − 20 °C for 20–30 min and centrifuged at 5000 rpm for 10 min at 4 °C. The aqueous and organic layers were combined, and supernatants were purified using preconditioned Amicon Ultra filters (0.5 mL) centrifuged at 15,000 rpm for 3 h at 4 °C. Filtrates were dried using a SpeedVac and reconstituted in 100 µL methanol: water (1:1, v/v), followed by vortexing, sonication (5 min), and centrifugation (15,000 rpm, 5 min). Supernatants were transferred to LC-MS vials. Metabolite profiling

was performed using an Agilent 6495 triple quadrupole LC/MS system in both ESI +/− modes. Chromatographic separation was employed using an Agilent SB-CN column (3 × 100 mm, 1.8 µm) with a flow rate of 0.3 mL/min. Solvent A was water + 0.1% formic acid; Solvent B was acetonitrile + 0.1% formic acid. The gradient ran from 15:85 (A: B) at 0–3 min to 98:2 at 12–16 min, returning to 15:85 at 28 min. Key MS parameters included: delta EMV 400 V, capillary voltage 3000 V, capillary temp 250 °C, sheath gas 350 °C at 12 units, and nebulizer pressure 20 psi. QC samples (liver and pooled) were run throughout each batch, with blanks (50:50 methanol: water) between injections to monitor carryover. Data were processed using Agilent MassHunter software. Peak areas were normalized to internal standards and log2-transformed. Statistical analysis was conducted using the R package.

Untargeted mass spectrometry

Samples for untargeted mass spectrometry were prepared as previously described and analyzed using a Thermo Scientific Vanquish Horizon UHPLC system coupled to a Thermo Scientific Orbitrap IQ-X Tribrid Mass Spectrometer [26]. Metabolite separation was performed via reversed-phase chromatography using HILIC, a Waters ACQUITY BEH Amide column. Appropriate solvent systems were used for each mode, with columns maintained at 50 °C, a flow rate of 300 µL/min, and 2 µL injection volume. Data acquisition was conducted in negative-ionization modes. Raw data were processed in Compound Discoverer (v3.3) for peak detection and annotation, using mzCloud, NIST 2020, HMDB, and an in-house retention time-matched library. Log2-transformed peak areas were normalized using the IQR method, and differential metabolites were identified based on $p < 0.05$. Metabolite set Enrichment Analysis was performed using www.metaboanalyst.ca [27].

Global methylation quantification

Global methylation was quantified using the Abcam Global DNA Methylation Assay Kit (5 Methyl Cytosine, Colorimetric). The methodology is described at the product website (ab117128). Briefly, it involves DNA isolation, fixation, antibody reaction, and detection using calorimetric methods.

Whole genome bisulfite sequencing and analysis

1 million cells were counted and used for Whole Genome Bisulfite Sequencing. Genomic DNA from the cells was extracted with Invitrogen™ PureLink™ Genomic DNA Mini Kit. Dual-indexed sequencing libraries were prepared from bisulfite-converted DNA using xGen™ Methyl-Seq DNA Library Prep Kit (Integrated DNA Technologies, Inc.) at the MDACC Epigenomics Profiling Core.

Briefly, 100ng of genomic DNA was fragmented in a Bioruptor® Pico sonication device (Diagenode Inc.) to an average of 350 bp, followed by bisulfite conversion using EZ DNA Methylation-Gold Kit (Zymo Research). Library preparation, comprising adaptase, extension, ligation, and indexing PCR steps, was performed according to the manufacturer's protocol. Libraries were quantified using Qubit 4 Fluorometer (ThermoFisher Scientific) and further evaluated for size and the presence of adapter-dimers using D1000 ScreenTape in a 4200 TapeStation System (Agilent). Libraries were sequenced on an NovaSeq X Plus 25B instrument at Novogene Corporation, Sacramento. Whole-genome bisulfite sequencing (WGBS) data were processed using a standard analysis pipeline. Raw FASTQ files underwent quality trimming with TrimGalore (v0.4.3) using default parameters. The trimmed reads were then aligned to the reference genome (hg38 for human samples) using Bismark (v0.18.1) [28]. The resulting BAM files were sorted by query name and deduplicated using Picard (v0.2.10.10), followed by coordinate sorting with Samtools (v1.9) [29].

Methylome extraction was performed with Bismark to generate coverage files from the aligned BAM files. These coverage files were used to construct an input file for DSS, containing four columns as specified in the DSS user manual: chromosome, CpG position, total read count, and number of methylated reads. Differentially methylated regions (DMRs) were identified using DSS [30], with a minimum DMR length of 50 bp and at least two CpG sites per region.

To functionally annotate the differentially methylated regions (DMRs) identified from WGBS data, we used the ChIPseeker package in R. DMR coordinates were first converted into GRanges objects using the GenomicRanges package. Annotation was then performed using the TxDb.H. sapiens. UCSC.hg38 known Gene transcript database and the org.Hs.eg.db annotation package for gene-level information. This allowed for the mapping of DMRs to genomic features such as promoters, exons, introns, and intergenic regions, providing biological context for methylation changes.

Invasion assay

Cell migration was evaluated using the MILLIPORE QCM™ 24-well Cell Migration Assay (ECM508, MilliporeSigma). A total of 5×10^4 cells were seeded in 300 µL of serum-free medium into the upper chamber of the insert. The lower chamber was filled with 500 µL of complete medium containing serum as a chemoattractant. Plates were incubated at 37 °C in a humidified atmosphere with 5% CO_2 for 4–24 h to facilitate cell migration. Post-incubation, non-migratory cells on the upper surface of the membrane were removed by aspirating the medium and gently swabbing the surface with sterile

cotton-tipped applicators. The inserts were then transferred into wells containing 400 µL of Cell Stain solution and incubated at room temperature for 20 min. Following staining, inserts were rinsed thoroughly by dipping in distilled water. Any residual non-migratory cells were removed using a second sterile cotton swab, ensuring the polycarbonate membrane remained intact. Inserts were then air-dried and transferred to wells containing 200 µL of Extraction Buffer. The stain was extracted by gently rocking the inserts for 15 min at room temperature. Subsequently, 100 µL of the extracted dye was transferred to a 96-well plate, and absorbance was measured at 560 nm using a microplate reader to quantify cell migration.

In Vivo study for metastasis

Twelve NSG castrated male mice (NOD.Cg-Prkdcscid Il2rgtm1Wjl/SzJ) were purchased from The Jackson Laboratory and randomly assigned into three groups ($n=4$ per group): DHODH-NT (non-targeting control), DHODH-KD (DHODH knockdown), and DHODH-Res (DHODH rescue). Each mouse was administered 1 million 22RV1 cells stably transduced with the respective constructs via intracardiac injection to assess metastatic dissemination in vivo. Metastasis was monitored using bioluminescent imaging. For imaging, 100 µL of D-luciferin (10 mg/mL) was administered via retro-orbital injection, and whole-body imaging was performed using the IVIS system with a 1-minute exposure time. All animals were imaged individually to assess tumor burden and metastatic spread. Body weights were recorded at regular intervals to monitor the animals' overall health and well-being. Mice were euthanized five weeks post-injection, or earlier if a strong bioluminescent signal indicative of metastatic burden was detected. The bioluminescent signal was Log Transformed. At the study endpoint, tissues and bones were collected, and the Human Tissue Acquisition and Pathology Core at Baylor College of Medicine evaluated metastatic lesions. The experiments and animal health assessments were conducted under the protocol approved by the Institutional Animal Care and Use Committee (IACUC) of Baylor College of Medicine (Protocol title: Integrative metabolomics of cancer detection and progression; Protocol number: AN-5676; Expiration date: 01/19/2029).

RADD assay

22RV1 and DHODH knockdown and rescue clones were seeded at 10,000 cells per well in 8-well ibidi chambers (ibidi GmbH, Grafelfing, Germany). Once cells reached 60% confluency, they were fixed with 4% paraformaldehyde. For the MDA-PCa-2b, the NT, DHODH knockdown, and rescue clones were grown to 70% confluency in a fibronectin-coated 10 cm dish. Cells were harvested with trypsin, resuspended in PBS, and counted. 100,000 cells were then spin-coated onto SuperFrost Plus slides (Fisher 22-037-246) using a Thermo Scientific Shandon Cytospin 4 Benchtop Centrifuge. Slides with the cells were subsequently fixed in 4% paraformaldehyde. 22RV1 and MDA-PCa-2b clones were then permeabilized with Biotium permeabilization buffer plus 0.05% Triton X-100 (Biotium, Fremont, CA). DNA lesions were enzymatically processed using a glycosylase/endonuclease cocktail for specific lesion types as previously described [1, 2]. For broad-spectrum DNA damage detection (Full RADD), uracil DNA glycosylase (UDG, New England Biolabs (NEB), M0280), formamidopyrimidine [fapy]-DNA glycosylase (FPG, NEB, M0240), T4 pyrimidine dimer glycosylase (T4PDG, NEB, M0308), human alkyladenine DNA glycosylase (AAG, NEB, M0313), endonuclease VIII (EndoVIII, NEB, M0299), and endonuclease IV (EndoIV, NEB, M0304) were added to the cells. Cells were incubated with the lesion removal mix for 1 h at 37 °C. Then, a gap-filling solution of Klenow exo (Thermo Fisher, EP0422) and digoxigenin-dUTP (Sigma Aldrich 11093088910) was added directly to the lesion removal solution and incubated for an additional 1 h at 37 °C. Cells were then washed three times in PBS for 5 min each and blocked in 2% BSA (Jackson Immuno, West Grove, PA, USA, 001-000-162) in PBS for 30 min at room temperature (RT, ~24 °C). After blocking, chambers are incubated with a primary antibody, anti-digoxigenin (1:250, ab420, Abcam) or an anti-mouse IgG1 isotype control (1:625, 5415, Cell Signaling), for 1 h at RT. IgG1 is used as a negative control. Once the primary antibody has finished incubation, the cells are washed three times with 1X PBS and incubated with the secondary antibody, anti-mouse AlexaFluor 546 (1:400, Thermo Fisher), for 1 h at RT. The cells are then incubated with Hoechst solution (1:800, Thermo Fisher) for 15 min at RT and washed three times with 1X PBS.

The chambers were stored in PBS, but the slides with the MDA-PCa-2b cells were mounted using Prolong Gold (Thermo Fisher). Cells are then imaged using the Keyence microscope with the 20X objective (NA 0.75). At least 30 cells from each condition in each biological replicate are counted across four different fields. For analysis, the Nikon Elements software created an ROI around the nucleus, and the total intensity for the RADD channel within the nucleus was recorded for at least 100 cells. The mean of the fluorescent intensity for all the nuclei over the four biological replicates was graphed in GraphPad Prism, and significance was calculated using an ANOVA with a Dunnett's post hoc test.

Clonogenic assay

Cells were plated in a 24-well plate at densities ranging from 250 to 8000 cells per well. The next day, cells were irradiated (0, 0.5, 1.5, 2, 2.5,3, 3.5, or 4 Gy). Six to 7 days

later, colonies were fixed with acetic acid/methanol (1:7, v/v), stained with crystal violet (0.5%, w/v), and counted using a stereomicroscope. Platting efficiency and DBAR (Dose-Based Area Ratio) were tabulated with ± SD. In a clonogenic survival curve, D bar is the mean lethal dose, representing the radiation dose required to reduce the surviving fraction of cells to 37% (1/e) in the exponential portion of the curve.

Results

DHODH expression is selectively elevated in prostate tumor epithelium and correlates with tumor malignancy

Analysis of the Cancer Genome Atlas (TCGA) Prostate Adenocarcinoma (PRAD) dataset showed a marked increase in DHODH mRNA levels in prostate tumor tissues ($n = 494$) compared with benign prostate samples ($n = 52$) ($p < 0.0001$, Wilcoxon test) (Fig. 1A). Independent validation using the Gene Expression Omnibus dataset (GSE70768) confirmed these results, indicating significantly higher DHODH expression in prostate tumors ($n = 125$) than in matched benign tissues ($n = 118$), further supporting DHODH's specific upregulation in malignant prostate tissue (Fig. 1B).

To establish a correlation between DHODH expression and tumor malignancy, we examined three additional transcriptomic datasets (GSE17951, GSE70768, and GSE8218). Across these independent cohorts, DHODH mRNA expression correlated positively with increased tumor cellularity, indicating preferential expression in regions with higher malignant content (Figs. 1C–E). Single-cell RNA sequencing analysis of prostate cancer biopsies (GSE141445; $n = 14$ patients) provided cell–type–specific expression patterns, providing further evidence of differential gene regulation across the tumor microenvironment. DHODH (dihydroorotate dehydrogenase) was found to be elevated in epithelial cells, indicating a selective enrichment of DHODH expression in the cell population within the prostate tumor milieu ($p < 0.001$, Wilcoxon test). This epithelial-specific overexpression suggests a potential role for DHODH in promoting tumor-associated epithelial cell functions or proliferation, thereby contributing to prostate cancer progression (Fig. 1F, Supplementary Figs. 1 A-D).

Notably, DHODH expression was higher in prostate tumors from African American (AA) patients compared to their European American (EA) counterparts ($p = 0.025$, Wilcoxon test, Supplementary Fig. 1E). This observation should be interpreted cautiously, given the limited number of AA samples in the TCGA dataset and the scarcity of comparable datasets to validate the finding. Previous in situ analyses conducted in our laboratory also identified higher accumulation of uracil and pyrimidine lesions, indicative of DNA repair activity, in tumors from AA patients compared with matched benign tissues [4]. These findings further implicate DHODH in the biological disparities observed across different patient populations.

Together, these data suggest that DHODH is selectively and significantly upregulated in prostate tumor epithelium, strongly associated with malignancy, and may play a role in the racial disparities seen in prostate cancer progression and outcomes. These findings identify DHODH as a promising biomarker and potential therapeutic target for prostate cancer.

Functional role of DHODH in prostate cancer cell proliferation through pyrimidine biosynthesis

To understand the biological importance of DHODH in prostate cancer, we created stable DHODH knockdown (KD) and overexpression (OE) models in two prostate cancer cell lines, 22RV1 (European American origin) and MDA-PCa-2b (African American origin), using lentiviral transduction [23]. Successful modulation of DHODH expression at both the RNA and protein levels was confirmed by quantitative PCR and Western blotting (Figs. 2A–F). Additionally, when compared to EA-derived 22RV1 cells, DHODH knockdown in AA-derived MDA-PCa-2b cells resulted in more effective protein suppression (Figs. 2B,C,E,F). Functionally, DHODH knockdown significantly reduced cellular proliferation, as shown by decreased BrdU incorporation (Figs. 2G**,** H). To test whether this effect depended on pyrimidine biosynthesis, rescue experiments were performed by adding exogenous uridine to DHODH-KD cells. This supplementation restored proliferation rates to levels similar to control cells (Fig. 2G), confirming DHODH's role in supporting cell growth through de novo pyrimidine biosynthesis. Overall, these findings show that disrupting DHODH in prostate cancer cells impairs proliferation by decreasing pyrimidine biosynthesis, and this effect is reversible with uridine supplementation.

DHODH depletion induces paradoxical enrichment of oxidative phosphorylation and compensatory mitochondrial adaptations

Transcriptomic profiling of MDA-PCa-2b cells with non-targeting control (NT), DHODH knockdown (KD), and rescue (KD2-Rescue) conditions identified significantly differentially expressed genes that change when DHODH is silenced and are restored when re-expressed (Fig. 3A). DHODH knockdown led to reduced expression of cell cycle genes, consistent with the decreased proliferation observed in growth assays (Fig. 3B). The significantly up-regulated genes were associated with metabolic re-programming, while down-regulated genes were associated with genomic instability (Figs. 3C**,** D).

DHODH functions as a vital metabolic link between nucleotide synthesis and mitochondrial respiration by

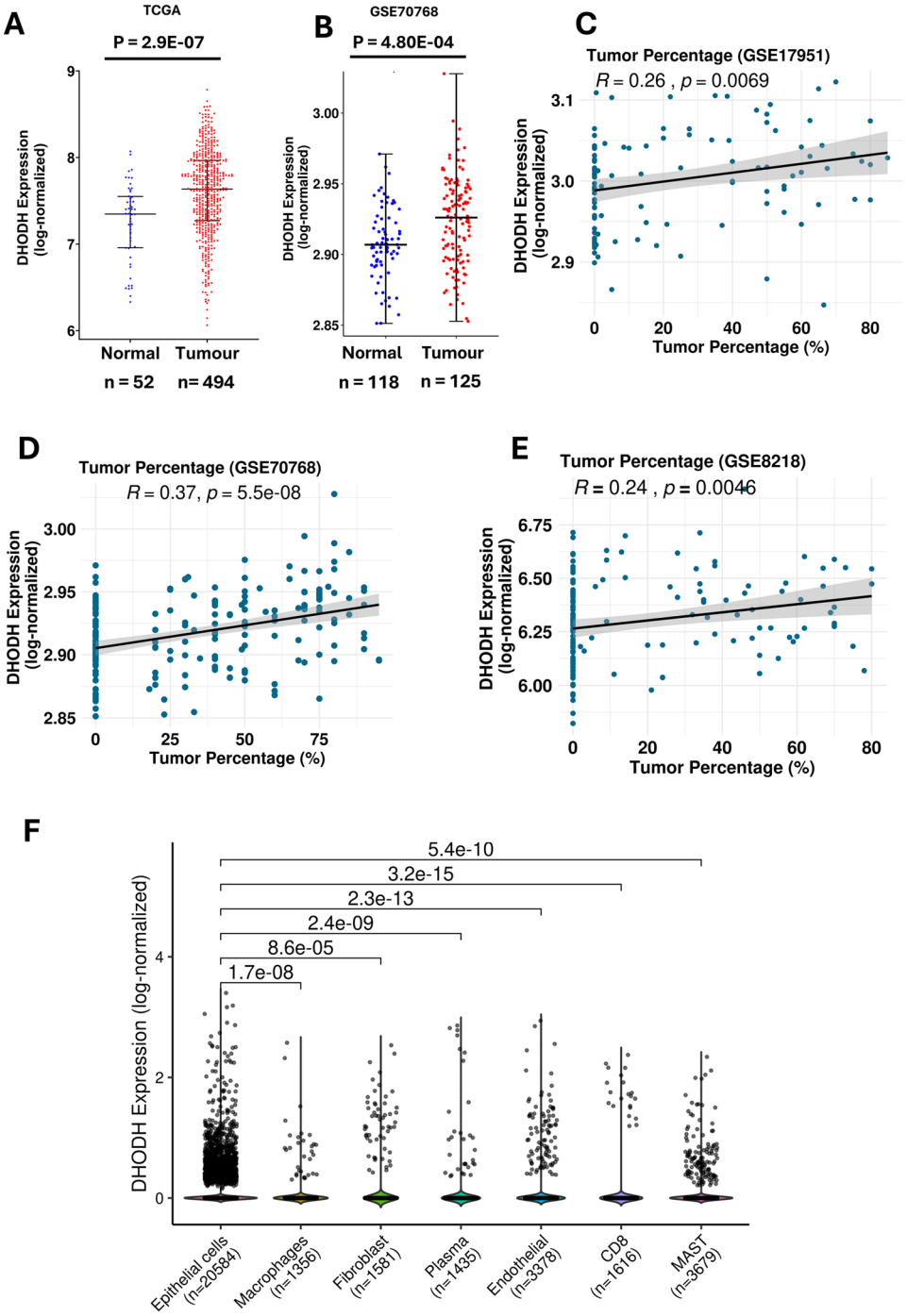

Fig. 1 Dihydroorotate Dehydrogenase (DHODH) is elevated in prostate cancer. **A** Dot plots showing elevated DHODH transcript levels in PCa compared to benign prostate tissue in the TCGA dataset [Prostate tumor tissues ($n = 494$), benign prostate samples ($n = 52$), P value using the Wilcoxon test]. **B** Dot plots showing elevated DHODH transcript levels in PCa compared to benign prostate tissue in an independent PCa data set GSE70768 [Prostate tumor tissues ($n = 125$), benign prostate samples ($n = 118$), P value using the Wilcoxon test. **C–E** Scatter plot showing a significant correlation between DHODH expression and the percentage of tumor in PCa across three independent datasets GSE17951, GSE70768, GSE8218 (Pearson correlation, p-value < 0.05). **F** Violin plot showing increased DHODH expression in tumor cells compared to other cell types in the tumor microenvironment in a scRNA-seq dataset containing 13 PCa tissues (GSE141445, P value using the Kruskal–Wallis test). Violin plots were generated using cell types with >20 DHODH-positive cells to ensure robust inference

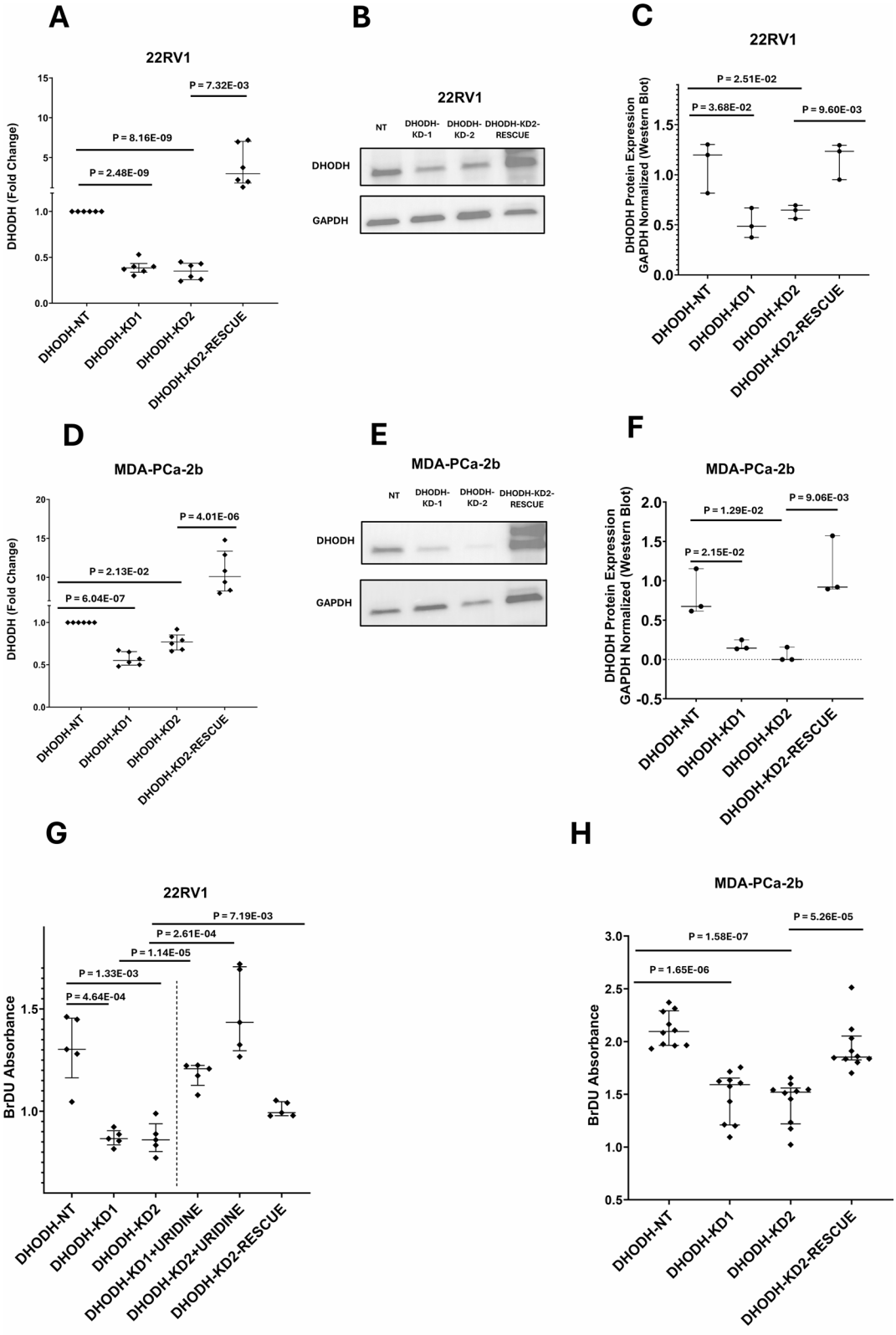

Figure 2

Fig. 2 (See legend on next page.)

(See figure on previous page.)

Fig. 2 Genetic knockdown of DHODH in PCa cell lines mitigates cell proliferation. **A** Dot plot representing mRNA expression of DHODH knockdown (KD) and rescue in 22RV1 cell lines [*n*= 6 (3 biological replicates with 2 technical replicates each), normalized by 18S expression, *P* value using Student's t-test]. **B** Immunoblot showing KD and rescue of DHODH in 22RV1 cells. **C** Quantification of the immunoblot in B normalized by GAPDH expression (*n* = 3 biological replicates, *P* value using Student's t-test). **D** Dot plot representing mRNA expression of DHODH of knockdown (KD) and rescue in MDA-PCa-2b cell lines [*n* = 6 (3 biological replicates with 2 technical replicates each), normalized by 18S expression, *P* value using Student's t-test]. **E** Immunoblot showing KD and rescue of DHODH in MDA-PCa-2b cells. **F** Quantification of the immunoblot in E normalized by GAPDH expression (*n* = 3 biological replicates, *P* value using Student's t-test). **G** Dot plot showing BrdU assay results representing reduced proliferation upon DHODH KD and rescued by DHODH re-expression in 22RV1 PCa cells (*n* = 5 biological replicates, *P* value using Student's t-test). Uridine addition to DHODH KD also rescued the proliferation. **H** Dot plot showing BrdU assay results representing reduced proliferation upon DHODH KD and rescued by DHODH re-expression in MDA-PCa-2b PCa cells. (*n* = 10, 5 biological replicates with 2 technical replicates each, *P* value using Student's t-test)

transferring electrons from dihydroorotate to ubiquinone within the electron transport chain (ETC). Located in the mitochondrial inner membrane, this reaction oxidizes dihydroorotate to orotate and produces ubiquinol, which directly supplies energy to Complex III and connects new pyrimidine biosynthesis with oxidative phosphorylation (OXPHOS) [31].

Paradoxically, transcriptomic analysis showed that knocking down DHODH led to a significant increase in OXPHOS pathways, along with higher expression of genes linked to glycolysis, the TCA cycle, and various ETC components, compared to both non-targeting controls and DHODH rescue re-expression (Figs. 4A**,** B; Supplementary Fig. 2A). This apparent boost in mitochondrial activity likely does not indicate improved bioenergetic efficiency. Instead, it points to a compensatory response to metabolic stress. When DHODH is lost, it disrupts the normal connection between pyrimidine biosynthesis and electron transfer in the ETC, causing a redox imbalance. This imbalance drives the cell to increase mitochondrial respiration and other metabolic processes to try to maintain energy balance.

Seahorse Mito Stress analysis further confirmed that DHODH-deficient cells have significantly higher oxygen consumption rates (OCR), indicating increased mitochondrial respiration as a stress response (Figs. 4C–E). Biochemical assays also showed heightened activity in mitochondrial respiratory Complexes II, and III after DHODH knockdown (Fig. 4F), supporting the connection between DHODH loss and compensatory electron transport chain (ETC) activation.

Consistent with disrupted mitochondrial redox balance, DHODH knockdown increased the $NADP^+$/NADPH and NAD^+/NADH ratios in both 22RV1 and MDA-PCa-2b cell lines, an effect fully reversed by DHODH re-expression (Figs. 4G**,** H; Supplementary Figs. 2B**,** C). Interestingly, the change in NAD: NADH ratio was more pronounced in MDA-PCa-2b AA cells compared to 22RV1 EA cells (Supplementary Fig. 2D). Moreover, cells lacking DHODH showed significantly higher reactive oxygen species (ROS) levels and increased mitochondrial DNA content (Figs. 4I**,** J; Supplementary Fig. 3), indicating oxidative stress and a compensatory increase in mitochondrial biogenesis.

Overall, depleting DHODH causes significant mitochondrial metabolic stress, disrupting redox balance and prompting compensatory increases in mitochondrial respiration, biogenesis, and metabolic flux. These adaptive responses highlight DHODH's crucial role in supporting mitochondrial function and metabolic stability—both essential for the survival and progression of prostate cancer cells.

DHODH depletion reprograms one-carbon metabolism, DNA methylation, and metastatic potential in prostate cancer

To explore the wider metabolic effects of DHODH deficiency, we conducted extensive untargeted and targeted metabolomic analyses (Supplementary Fig. 4 and Figs. 5A–E). Global metabolomics revealed a notable increase in methylation-related pathways in DHODH-deficient cells (Fig. 5A). These changes were confirmed by targeted mass spectrometry, which showed higher intracellular levels of methionine and homocysteine (Figs. 5B–E), key metabolites of the one-carbon cycle. Since the one-carbon cycle is crucial for producing S-adenosylmethionine (SAM) for methylation processes and supporting pyrimidine synthesis, these results imply a compensatory enhancement of this pathway to maintain vital biosynthesis when DHODH activity is compromised.

In line with altered methylation , DHODH knockdown cells showed notably higher global DNA methylation relative to controls (Figs. 5F**,** G). Quantitative PCR revealed a notable reduction in Ten-Eleven Translocation isoform 1 and 2 (TET1 and TET2) expressions, an enzyme crucial for active DNA demethylation, in DHODH-deficient cells (Figs. 5H**,** I). This likely reduces DNA demethylation activity, contributing to the observed global hypermethylation.

To explore effects at specific loci, whole-genome bisulfite sequencing (WGBS) was conducted on DHODH knockdown and NT control MDA-PCa-2b cells, identifying distinct differentially methylated regions (DMRs) that span both hyper- and hypomethylated gene loci (Fig. 5J). Pathway enrichment analysis of hyper-methylated genes associated with these DMRs indicated significant involvement in epithelial–mesenchymal transition

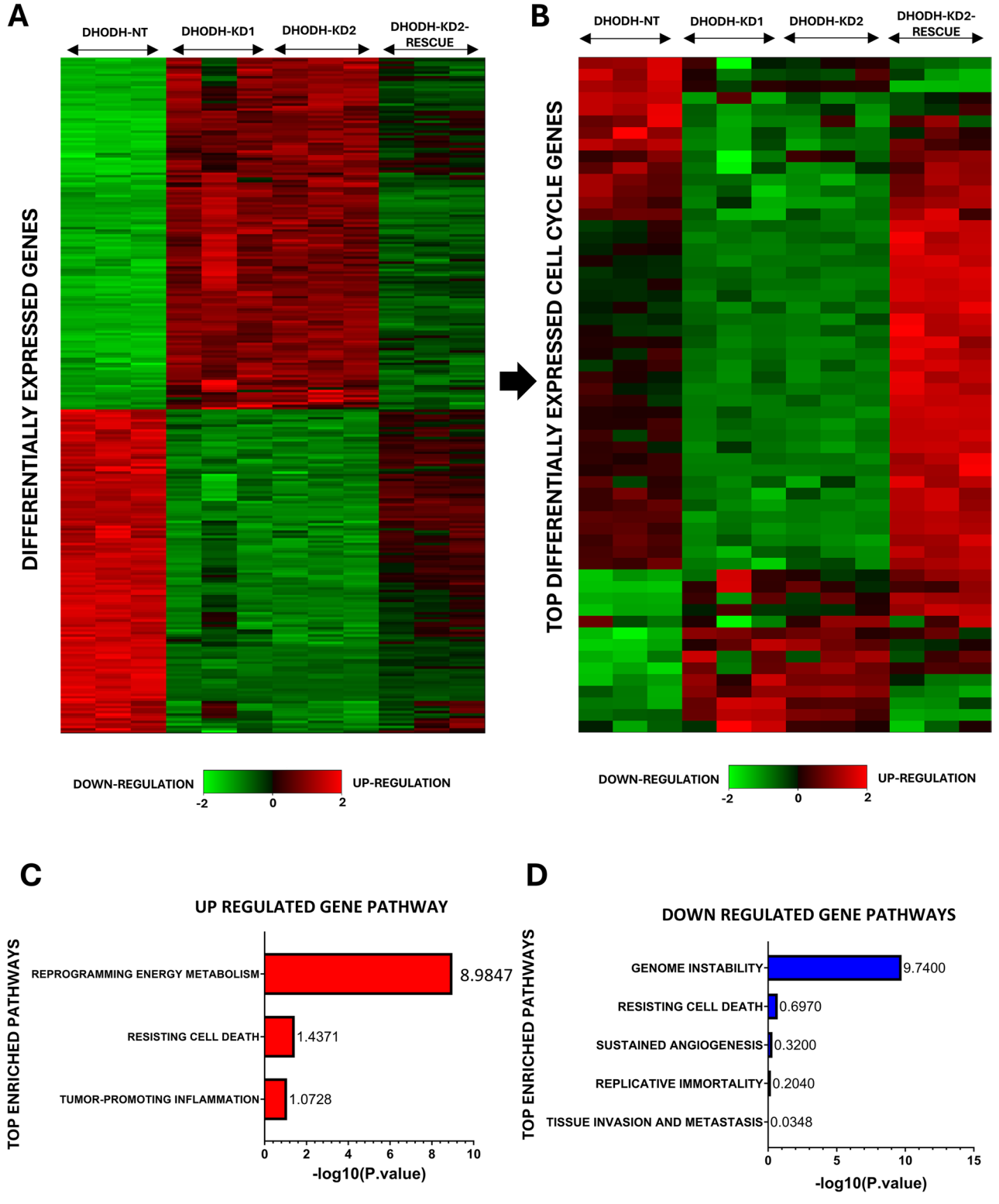

Fig. 3 (See legend on next page.)

(See figure on previous page.)

Fig. 3 Transcriptomic analysis reveals a decrease in the cell cycle and an increase in energy metabolism following DHODH knockdown (KD) in MDA-PCa-2b prostate cancer cells. **A** Heat map showing differentially expressed genes identified by bulk RNA sequencing, comparing DHODH KD to non-targeting (NT) control and DHODH rescue. The green color represents significantly down-regulated genes, and red represents up-regulated genes (n = 3 biological replicates, $P < 0.05$, FDR=0.25). **B** Heat map showing subset of differentially expressed cell cycle-associated genes identified by bulk RNA sequencing, comparing DHODH KD to non-targeting (NT) control and DHODH rescue. The green color represents significantly down-regulated genes and red represents up-regulated genes (n = 3 biological replicates). This subset of differentially expressed genes ($P < 0.05$) at an FDR threshold of 0.25 was derived from Fig. 3A. **C** Bar graph illustrating Hallmark Pathways linked to upregulated genes from transcriptomics analysis of DHODH KD versus NT. The -Log10 (*P*) value is shown on the X-axis. **D** Bar graph illustrating Hallmark Pathways linked to downregulated genes from transcriptomics analysis of DHODH KD versus NT. The -Log10 (*P*) value is shown on the X-axis

(EMT) and inflammatory signaling pathways (Fig. 5K), implying that metabolic alterations driven by DHODH can directly modulate the epigenetic regulation of key cancer-related transcriptional programs. Functional assays supported these molecular findings. In vitro trans well migration tests showed a significant decrease in migration in DHODH-deficient cells (Fig. 5L).

Considering the known connection between EMT and metastasis, we assessed in vivo metastasis using an intracardiac injection model in immunocompromised castrated NSG mice. Bioluminescent IVIS imaging showed a marked decrease in metastatic spread—measured by luminescence intensity—in mice injected with DHODH-knockdown cells compared with controls. Further, H&E staining confirmed metastatic lesions in 50% of animals from the NT and Rescue group, while none of the animals injected with DHODH-KD showed metastasis (Fig. 5M; Supplementary Figs. 5 A, B).

Overall, these findings demonstrate that DHODH depletion reprograms the one-carbon cycle, altering DNA methylation patterns and EMT-related gene expression. This results in decreased migratory behavior in vitro and a lower metastatic potential in vivo. These findings highlight DHODH's crucial role in linking metabolic and epigenetic networks that drive aggressive prostate cancer, underscoring its potential as a therapeutic target.

DHODH depletion impairs DNA repair pathways, increases DNA damage, and influences treatment outcomes

To explore how DHODH depletion affects DNA repair, we analyzed the transcript levels of key DNA repair genes. Knockdown of DHODH significantly lowered the expression of genes involved in mismatch repair, base excision repair (BER), and nucleotide excision repair (NER) (Figs. 6A–C), indicating a widespread disruption of high-fidelity repair pathways. Interestingly, some genes within the BER and NER pathway were upregulated, like MPG, SMUG1, and PARP4 for BER and RBX1 and RAD23 for NER, were upregulated when DHODH was lost. RAD23 is critical for assembly during NER repair, and also acts to enhance protein stability of repair complexes, including through interactions with Y-family of DNA polymerases [32] .

Concurrently, a subset of genes from the Y-family of DNA polymerases—responsible for trans-lesion synthesis were upregulated, notably REV3L (Fig. 6D, Supplementary Figs. 6A–F). This suggests an adaptive, albeit error-prone, mechanism to bypass unrepaired DNA damage. Notably, even with an overall decrease in canonical repair transcripts, the BER factors PARP1 and XRCC1 showed increased levels in DHODH-knockdown cells compared to non-targeting (NT) (Supplementary Figs. 6G, H).

Consistent with impaired repair ability, the Repair Assisted Damage Detection (RADD) assay revealed a significant rise in the broad-spectrum DNA damage signal (Full RADD) in DHODH-deficient cells compared to non-targeting (NT) and rescue controls (Figs. 6E, F), indicating a greater amount of unrepaired DNA damage when DHODH is lost.

Functional clonogenic assays showed that DHODH knockdown cells had a significantly higher plating efficiency compared to NT and rescue controls (Fig. 6G). They also displayed a trend toward a higher dose–based area ratio (DBAR; Supplementary Fig. 6I), suggesting better colony formation under stress. This surprising increase in clonogenic survival, despite increased DNA damage, likely indicates a shift toward lesion tolerance rather than repair accuracy. This may enable damaged cells to survive and accumulate mutations.

The above findings suggest DHODH depletion reduces nucleotide pools, leading to replication stress and single-strand breaks. This activates PARP1 signaling and attracts XRCC1 to stabilize and restart stalled forks. The increased RADD signal, induction of Y-family polymerases, and maintained clonogenic growth under stress support a model in which cells prioritize lesion tolerance and quick fork restart over high-fidelity repair.

Prostate cancer patient data demonstrate the clinical importance of these DNA repair defects. Prostate cancer patients receiving combined radiotherapy and androgen deprivation therapy (ADT) with low DHODH expression had notably shorter biochemical recurrence–free survival compared to those with high DHODH levels (Fig. 6H). This finding aligns with experimental results: tumors with diminished DHODH may have compromised DNA repair, leading to greater genomic instability and reduced long-term effectiveness of DNA-damaging therapies.

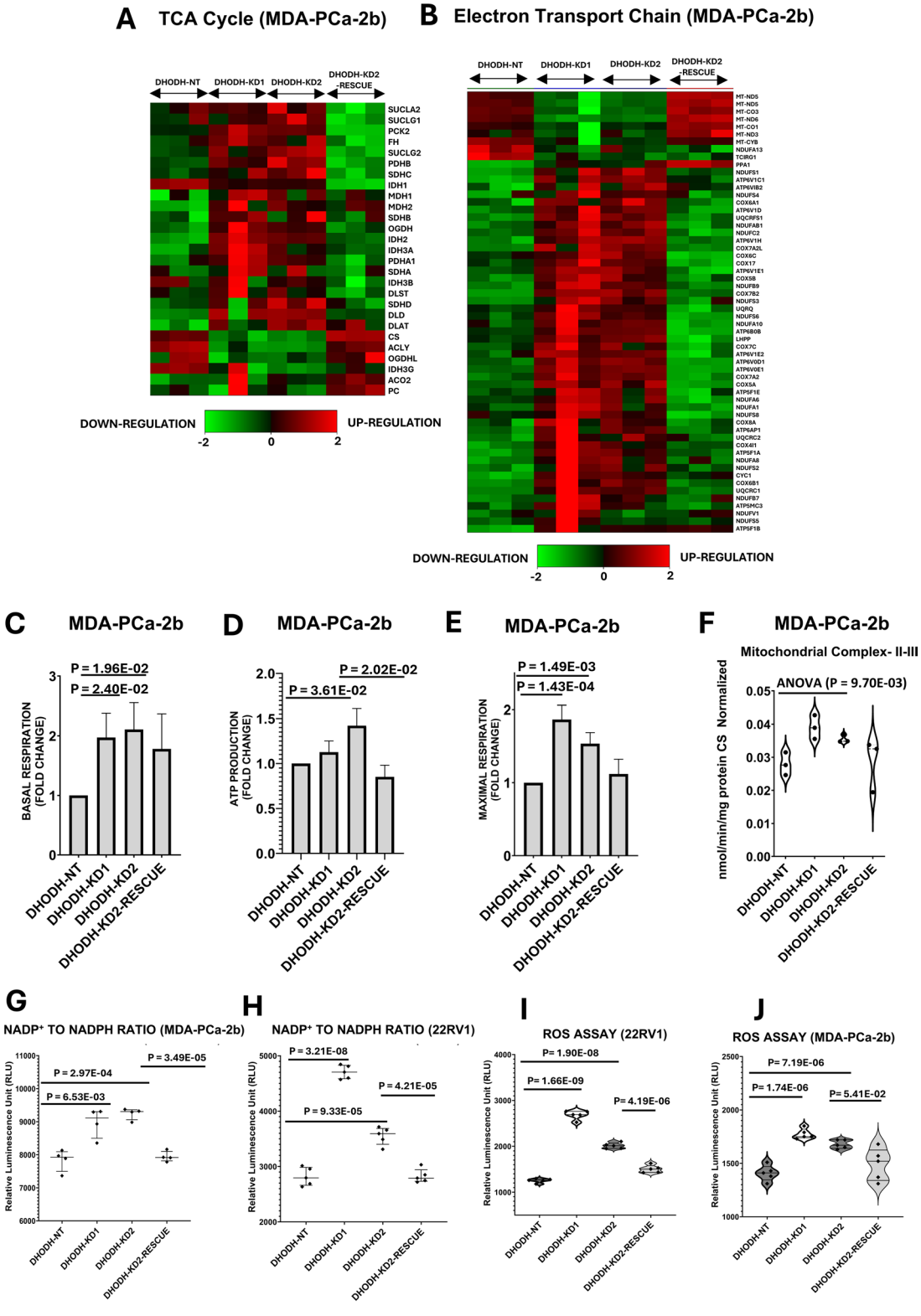

Figure 4

Fig. 4 (See legend on next page.)

(See figure on previous page.)

Fig. 4 KD of DHODH increases mitochondrial activity and bioenergetics in PCa cell lines. **A**, **B** Heat map illustrating the expression levels of a subset of genes associated with the TCA Cycle and the Electron Transport Chain (ETC). The green color represents significantly down-regulated genes, and red represents up-regulated genes (n = 3 biological replicates). This subset of differentially expressed genes ($P < 0.05$) at an FDR threshold of 0.25 was derived from Fig. 3A. **C–E** Seahorse analysis shows increased Basal Respiration, ATP Production, and Maximal Respiration in DHODH KD compared to NT or rescue controls. ($n = 15$, 3 biological replicates and 5 technical replicates per run). **F** Activity of mitochondrial electron transport chain complexes II-III is elevated upon KD of DHODH in MDA-PCa-2b cells (n = 3 biological replicates, *P* value using ANOVA). **G**, **H** Dot plot representing increased $NADP^+$: NADPH ratios in MDA-PCa-2b and 22RV1 DHODH KD compared to NT and rescue controls (n = 4-5 biological replicates, *P* value using Student's t-test). **I**, **J** Violin plot representing increased Reactive Oxygen Species (ROS) in 22RV1 and MDA-PCa-2b DHODH KD compared to NT and rescue controls ($n = 4$-5 biological replicates, *P* value using Student's t-test)

Together, these findings identify DHODH as a crucial factor in maintaining genomic stability in prostate cancer. When lost, it hampers multiple repair pathways, leads to dependence on error-prone polymerases, boosts DNA damage, and correlates with poorer treatment results. This underscores DHODH's role in driving repair deficiencies and its potential as a biomarker for therapeutic response.

Discussion

Prostate cancer (PCa) remains a leading cause of cancer-related illness and death among African American (AA) men, who face a higher rate of aggressive diseasecompared to European American (EA) men [33]. Our earlier transcriptomics and DNA damage studies showed increased uracil incorporation and pyrimidine-related DNA damage in prostate tumors from AA patients, indicating deficiencies in nucleotide metabolism and DNA repair mechanisms [4]. In this research, we highlight dihydroorotate dehydrogenase (DHODH)—a crucial enzyme in de novo pyrimidine synthesis [11] as a key regulator of metabolism, epigenetic changes, and genomic stability in prostate cancer.

Analysis of independent transcriptomic datasets, including TCGA-PRAD and GEO cohorts, revealed that DHODH expression was consistently higher in prostate tumors than in benign tissues and correlated positively with tumor cellularity. Single-cell RNA sequencing localized DHODH overexpression to tumor epithelial cells, which are closely linked to tumor initiation, progression, and metastasis [34]. Importantly, in a small patient cohort within the TCGA, DHODH levels were found to be elevated in tumors from African American (AA) patients compared to European American (EA) patients, suggesting the presence of race-specific molecular and metabolic signatures [4, 5, 7].

Functionally, DHODH is crucial for maintaining prostate cancer cell growth via its primary role in pyrimidine biosynthesis. Knocking down DHODH decreased cell proliferation, which was fully restored by adding exogenous uridine, highlighting the enzyme's metabolic dependence—consistent with previous findings in other cancers [35]. Our results are also consistent with previous in vivo tumor studies [36]. Besides its role in nucleotide synthesis, the loss of DHODH disrupted its connection to mitochondrial respiration, unexpectedly boosting oxidative phosphorylation (OXPHOS) pathways and enhancing activity in mitochondrial respiratory complexes II, and III. Seahorse assays and biochemical tests showed increased oxygen consumption, higher $NADP^+$/NADPH ratios, higher reactive oxygen species (ROS) levels, and mitochondrial biogenesis, indicating a compensatory response to metabolic stress [37].

This mitochondrial stress reprogramming extended to one-carbon metabolism. Targeted and untargeted metabolomics revealed elevated levels of methionine and homocysteine, indicating compensatory upregulation of the one-carbon cycle to support biosynthesis and methylation. Knockdown of DHODH led to global DNA hypermethylation, likely due to decreased expression of TET1 and TET2 and reduced active DNA demethylation, aligning with emerging evidence linking mitochondrial metabolism to nuclear methylation regulation [38, 39].

TET enzyme activity is controlled at the transcriptional, post-translational, and metabolic levels. Inhibition of dihydroorotate dehydrogenase (DHODH) disrupts electron transfer, thereby impairing respiratory efficiency [11]. This disruption triggers a compensatory increase in oxidative phosphorylation and mitochondrial biogenesis, disturbing the $NADP^+$/NADPH redox balance and increasing reactive oxygen species (ROS) production. A reduction in cellular NADPH hampers the maintenance of ferrous iron (Fe^{2+}) within the catalytic site of TET dioxygenases, leading to a loss of enzyme activity [40]. Besides its role in metabolic regulation, oxidative stress and NADPH depletion can also affect transcriptional networks by modulating redox-sensitive transcription factors like the androgen receptor (AR) [41]. Elevated mitochondrial ROS can impair AR signaling in prostate cancer, reducing receptor stability and nuclear activity [42]. Moreover, TET2 activity is implicated in regulating androgen-dependent transcriptional repression mechanisms in prostate cancer, underscoring a key connection between epigenetic and transcriptional landscapes [43]. These findings highlight a mechanistic link between metabolic dysfunction, epigenetic dysregulation, and transcriptional reprogramming in prostate tumor development.

Importantly, whole-genome bisulfite sequencing identified regions with differential methylation, especially

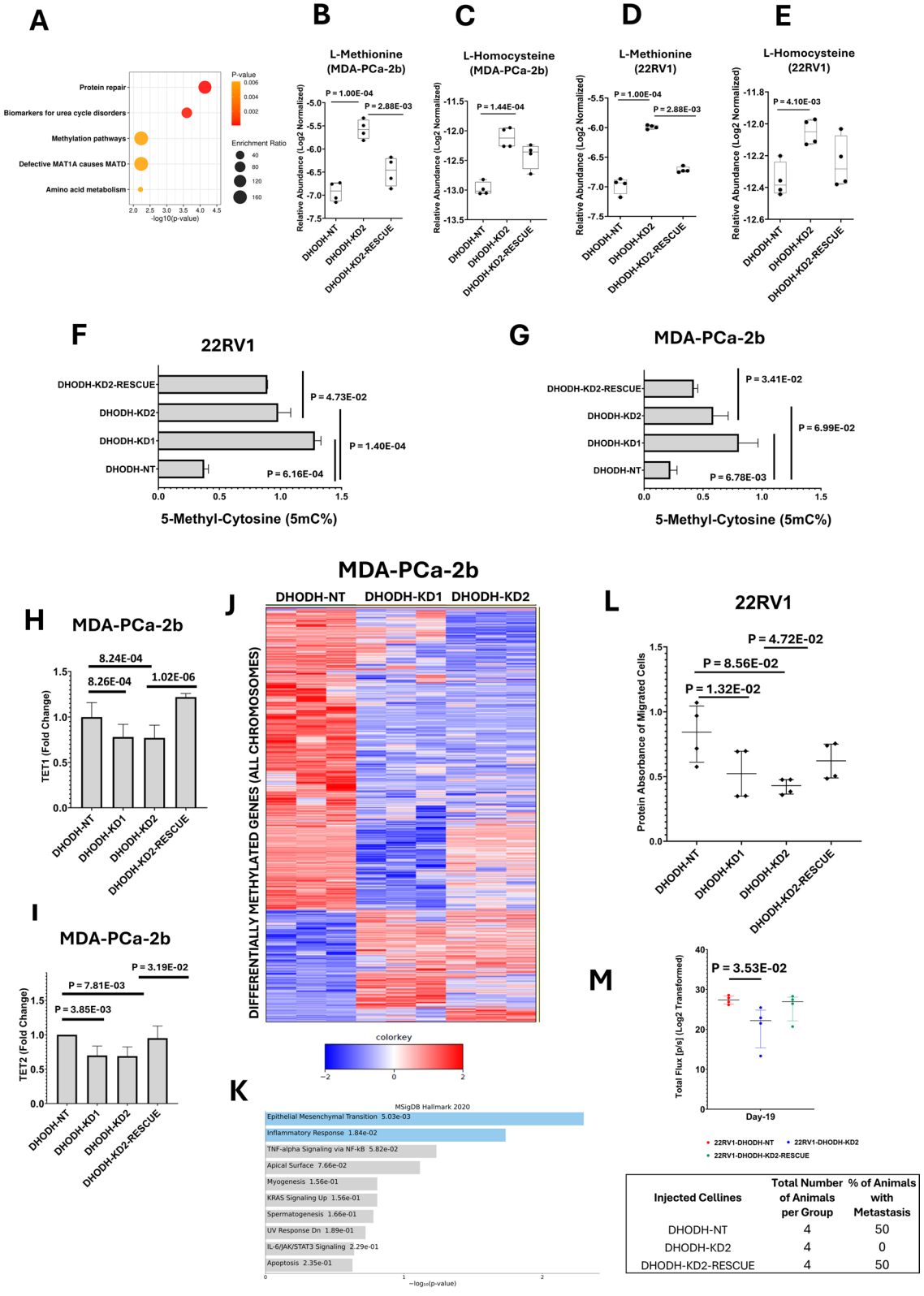

Injected Cellines	Total Number of Animals per Group	% of Animals with Metastasis
DHODH-NT	4	50
DHODH-KD2	4	0
DHODH-KD2-RESCUE	4	50

Figure 5

Fig. 5 (See legend on next page.)

(See figure on previous page.)

Fig. 5 DHODH KD in PCa cells results in perturbation of DNA methylation. **A** Metabolite-Set Enrichment Analysis (MSEA, FDR<0.1) of unbiased metabolic profiles in 22RV1-DHODH KD cell lines reveals changes in methylation pathways. Metabolite Set Enrichment Analysis (MSEA) was performed using the RaMP-Database (integrated KEGG, HMDB, Reactome, WikiPathways, and conducted using the online MetaboAnalyst program). Shades of red indicate higher significance, and larger dots represent higher enrichment ratios. **B–E** Box plots showing increased levels of the one-carbon metabolites homocysteine and methionine in DHODH KD compared to NT and rescue in MDA-PCa-2b and 22RV1 cells ($n = 3$ biological replicates, P value using Student's t-test). **F** Bar plots illustrating 5mC% in control, DHODH KD, and rescue in 22RV1 cells ($n = 3$ biological replicates, P value using Student's t-test). **G** Bar plots illustrating 5mC% in control, DHODH KD, and rescue in MDA-PCa-2b cells ($n = 3$ biological replicates, P value using Student's t-test). **H** Bar graphs showing relative mRNA expression levels of TET1 enzyme in MDA-PCa-2b cellines determined by qPCR ($n = 3$ biological replicates, normalized by Beta-Actin, P value using Student's t-test). **I** Bar graph representing qPCR results of TET2 for MDA-PCa-2b cell lines (n = 3 biological replicates, normalized by Beta-Actin, P value using Student's T-test). **J** Heat map displaying differentially methylated genes identified through whole-genome bisulfite sequencing of MDA-PCa-2b cells with NT andDHODH KD, ($n = 3$ biological replicates, $p < 0.05$, FDR < 0.25). Shades of red and blue indicate hypermethylated and hypomethylated genes, respectively. **K** Pathways related to epithelial-mesenchymal transition (EMT) and inflammatory responses were significantly enriched among the hypermethylated genes in DHODH KD compared to NT and DHODH rescue ($p < 0.05$). Pathway enrichment analysis was performed using Enrichr and the Hallmark database. **L** Dot plot representing quantification of trans well invasion assay showing reduced invasion in 22RV1 cells containing DHODH KD compared to NT and rescue ($n = 4$) biological replicates, P value using Student's t-test. **M** Dot plot showing reduced metastasis in 22RV1 mouse tumors with DHODH KD compared to NT and DHODH rescue on Day 19 post-intracardiac injection. Metastasis was quantified using luciferase by IVIS imaging ($n = 4$ animals per group, P value using Student's t-test). Each dot is an aggregate signal per animal in the group on Day 19. The table shows the percentage of metastasis observed within each experimental group

in genes involved in epithelial–mesenchymal transition (EMT) and inflammatory signaling. These epigenetic modifications were functionally associated with decreased cell migration in vitro, a shift toward an epithelial phenotype, and a significant reduction in metastatic potential in vivo, supporting previous studies linking metabolic dysfunction to reduced metastatic capacity [44].

Our integrative analysis of methylome and transcriptome data showed that depleting DHODH hinders several high-fidelity DNA repair pathways, such as mismatch repair, base excision repair (BER), and nucleotide excision repair (NER). Simultaneously, subset of genes for Y-family DNA polymerases—which are involved in error-prone trans lesion synthesis—were upregulated, pointing to a shift toward lesion tolerance. The Repair Assisted Damage Detection (RADD) assay confirmed an increase in DNA damage. In contrast, clonogenic assays unexpectedly demonstrated enhanced colony formation under stress, potentially due to the survival of genomically unstable cells. Clinically, patients with low DHODH expression receiving combined radiotherapy and androgen deprivation therapy (ADT) experienced significantly shorter biochemical recurrence–free survival, implying that repair deficits associated with DHODH deficiency led to decreased sensitivity to DNA-damaging treatments [4, 45].

Our results identify DHODH as a versatile key regulator in prostate cancer development. Its roles go beyond pyrimidine production, including regulation of mitochondrial function, redox homeostasis, one-carbon metabolism, and epigenetic modifications, all of which influence tumor growth, metastatic potential, and genomic stability. It also plays a paradoxical role in overcoming radiation stress and promoting cell survival.

Significance and future directions

Our study identifies dihydroorotate dehydrogenase (DHODH) as a key metabolic–epigenetic–genomic hub in prostate cancer, coordinating nucleotide availability with mitochondrial redox balance, chromatin configuration, and DNA damage responses. Loss of DHODH results in compensatory mitochondrial changes, including increased oxidative phosphorylation, increased oxygen consumption, and elevated electron transport chain activity, along with disrupted redox homeostasis. It also causes rewiring of one-carbon metabolism and DNA methylation pathways that influence EMT and inflammatory signaling. These epigenetic alterations lead to a phenotype that is more epithelial and less motile, with decreased invasion and metastasis observed in vivo. Additionally, DHODH depletion reduces high-fidelity DNA repair mechanisms (MMR/BER/NER) while increasing trans-lesion synthesis, which raises DNA damage but unexpectedly enhances clonogenic survival under genotoxic stress. Clinically, low DHODH levels are linked to shorter recurrence-free survival after RT + ADT, suggesting its value as a marker for treatment persistence rather than metastasis potential, highlighting the importance of personalized therapeutic approaches.

These data resolve a seeming paradox—metastasis decreases while treatment persistence rises when DHODH levels are low—by presenting a unifying model: decreased de novo pyrimidine flux disconnects mitochondrial electron transfer, leading to a slow-cycling, OXPHOS-dependent, lesion-tolerant state that reduces radiation lethality (which relies on damage fixation and precise repair during proliferation). Androgen deprivation likely strengthens this persister-like program by further limiting cell-cycle progression and promoting oxidative metabolism, accounting for the poorer RT + ADT outcomes seen in DHODH-low tumors. The finding that uridine restores proliferation highlights the key role of pyrimidine flux in this transition.

Looking ahead, this model highlights key testable priorities. First, boost radiation effects in DHODH-low

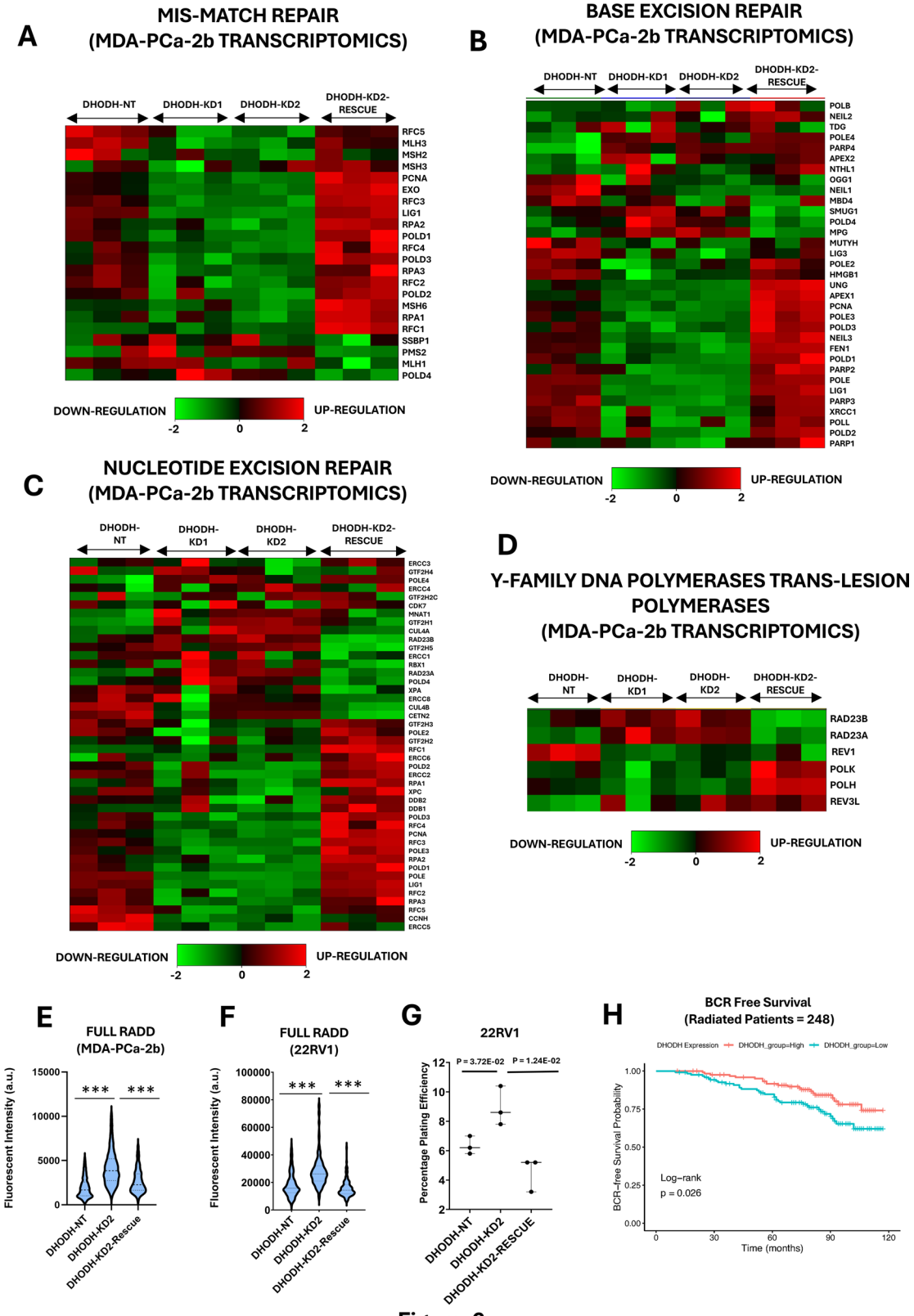

Figure 6

Fig. 6 (See legend on next page.)

(See figure on previous page.)

Fig. 6 DHODH depletion impairs DNA repair pathways, increases DNA damage, and influences treatment outcomes. **A** Heat showing differentially expressed subset of mismatch repair genes identified by bulk RNA sequencing, comparing DHODH KD to non-targeting (NT) control and DHODH rescue in MDA-PCa-2b cells. The green color represents significantly down-regulated genes, and red represents up-regulated genes ($n = 3$ biological replicates). This subset of differentially expressed genes ($P < 0.05$) at an FDR threshold of 0.25 was derived from Fig. 3A. **B** Heat showing subset of differentially expressed base excision repair genes identified by bulk RNA sequencing, comparing DHODH KD to non-targeting (NT) control and DHODH rescue in MDA-PCa-2b cells. The green color represents significantly down-regulated genes, and red represents up-regulated genes (n = 3 biological replicates). This subset of differentially expressed genes ($P < 0.05$) at an FDR threshold of 0.25 was derived from Fig. 3A. **C** Heat showing subset of differentially expressed nucleotide excision repair genes identified by bulk RNA sequencing, comparing DHODH KD to non-targeting (NT) control and DHODH rescue in MDA-PCa-2b cells. The green color represents significantly down-regulated genes, and red represents up-regulated genes ($n = 3$ biological replicates). This subset of differentially expressed genes ($P < 0.05$) at an FDR threshold of 0.25 was derived from Fig. 3A. **D** Heat showing subset of differentially expressed trans-lesion polymerases identified by bulk RNA sequencing, comparing DHODH KD to non-targeting (NT) control and DHODH rescue in MDA-PCa-2b cells. The green color represents significantly down-regulated genes, and red represents up-regulated genes (n = 3 biological replicates). This subset of differentially expressed genes ($P < 0.05$) at an FDR threshold of 0.25 was derived from Fig. 3A. **E** Violin plots showing the quantification of DNA damage detected by RADD assay in DHODH NT, KD, KD rescue in MDA-PCa-2b cells ($n = 3$ biological replicates, *** represents $P < 0.001$ obtained using ANOVA with a Dunnett's post hoc test). **F** Violin plots showing the quantification of DNA damage detected by RADD assay in DHODH NT, KD, KD rescue in 22RV1 cells ($n = 3$ biological replicates, *** represents $P < 0.001$ obtained using ANOVA with a Dunnett's post hoc test). **G** Dot plot representing percentage clonogenic assay plating efficiency of DHODH KD compared to NT and DHODH rescue in 22RV1 cells ($n = 3$ biological replicates, P value using Student's t-test). **H** Survival plot representing BCR-free survival between DHODH High and Low patients (Time period after radiation treatment during which a patient experiences no biochemical recurrence) obtained from 248 localized/locally advanced prostate cancer patients (GSE116918)

tumors by combining radiotherapy (RT) with DNA-damage response inhibitors like ATR/CHK1 or PARP inhibitors, and, where possible, agents that inhibit trans lesion synthesis (REV1–REV7), to reduce fork tolerance and induce lethal damage. Second, address the metabolic basis of persistence by inhibiting mitochondrial oxidative phosphorylation and electron transport (OXPHOS/ETC). Third, improve treatment sequencing by administering RT during cell-cycle re-entry or providing DDR blockade immediately prior. Fourth, stratify clinical trials based on DHODH status: DHODH-low cases might benefit from RT combined with DDR therapy for sustained local control. At the same time, DHODH-targeted strategies may be better suited for minimal residual or micro metastatic disease when paired with anti-tolerance or anti-OXPHOS agents. These hypotheses should be tested in vivo using RT + ADT models with quantitative endpoints, such as cell quiescence and double-strand break repair kinetics, including perturbations, such as uridine supplementation or transient ETC modulation, to establish causality, while ensuring evaluation across diverse patient populations. Collectively, our findings highlight the multifaceted role of DHODH in prostate cancer development and the radiation-response mechanisms promoting cell survival. One limitation of this study is the reliance on cell lines for epigenetic, transcriptomic, and metabolic analyses. While these results provide valuable insights, additional in vivo studies are needed to clarify the role of DHODH within a complex tumor microenvironment. Furthermore, access to larger RNA-seq cohorts from African American prostate cancer patients with extended clinical follow-up will help establish the clinical significance of DHODH in the context of prostate cancer health disparities.

Supplementary Information

The online version contains supplementary material available at https://doi.org/10.1186/s12964-026-02691-9.

Supplementary Material 1

Acknowledgments

The authors acknowledge the Agilent Global Center for Mass Spectrometry Excellence at BCM and the MDACC Epigenomics Profiling Core at MD Anderson Cancer Center. The MDACC Epigenomics Profiling Core is supported in part by The University of Texas MD Anderson Cancer Center and the Center for Cancer Epigenetics. The Charles C Bell Jr.-Endowed professorship supports Dr. Sreekumar. We acknowledge the following grants DoD W81XWH2210135 (ASK, NG), DoD HT94252510160 (NG), Dan L. Duncan Cancer Center P20CA284971 (ASK and NP), NCI Cancer Center Support Grant P30CA125123 [Metabolomics (NP, ASK) and HTAP (MI)], National Cancer Institute R01CA267090 (ASK), National Cancer Institute 5R01CA227559 (ASK), NIH/NCI R01CA282282 (NP), Cancer Prevention & Research Institute of Texas Proteomics & Metabolomics Core Facility Support Award CPRIT RP210227 (NP, ASK, VP), NIH S10OD032218 (ASK) and NIH P30 CA125123 (VP) Cancer Prevention Research Institute of Texas (CPRIT), RR180061 (CCO) and National Institutes of Health R01CA269764 (CCO). SLG and CCA were partially supported by CPRIT RP210227 and RP250580, NIH/NCI P30 shared resource grant CA125123, NIH/NIEHS P42 ES027725 and P30 ES030285, NIH/NCI U54 CA274321 and R21 DE032344, and S10 OD032185.This research was also partially funded by the NIH and DOD, with grants awarded to M.K.N. under grant number R01CA248310 and LC210305, respectively.

Authors' contributions

SR: Design, Procedure, data compilation, analysis, writing-original draft preparation, DWBP: Methylation and RNA sequencing Data Analysis, VM and CCO: Single Cell sequencing and transcriptomic data analysis. UR: Model system development and validation, VV, KRKR: Animal Experiment, MI: Histopathology, JHP, BAK: Mitochondrial Studies, VP, NP, SMT: Mass Spectrometry, SLG, CCA, JAJ: Data Integration, KG, TM, NRG, MKN, RKM: DNA damage studies, ASK: conceptualization, investigation, methodology, writing-original draft preparation, supervision, resources, data curation, and validation.

Data availability

Gene expression datasets for Prostate Adenocarcinoma (PRAD) were obtained from multiple sources. TCGA-PRAD samples and corresponding clinical information were downloaded from the Broad Institute's FireBrowse portal (http://firebrowse.org). In addition to the TCGA dataset, publicly available gene expression profiles were retrieved from the Gene Expression Omnibus

(GEO) under the accession numbers GSE70768, GSE17951, GSE8218, and GSE116918. The code used for the processing and analysis of bulk RNA-seq data is available on GitHub. [https://github.com/venu887/DHODH_Prostate_Cancer](https:/github.com/venu887/DHODH_Prostate_Cancer) . Single-cell RNA sequencing (scRNA-seq) data were also obtained from the Gene Expression Omnibus (GEO) under accession number GSE141445. The code for reproducing and analyzing the scRNA-seq data is available on GitHub: [https://github.com/venu887/DHODH_Prostate_Cancer](https:/github.com/venu887/DHODH_Prostate_Cancer) . The raw transcriptomic data have been deposited in [NCBI](https://www.ncbi.nlm.nih.gov/geo) GEO under the ID (GSE305522).

Declarations

Ethics approval and consent to participate

Animal experiments were carried out and the health of the mice was monitored per the animal protocol approved by the Institutional Animal Care and Use Committee (IACUC) of Baylor College of Medicine (Protocol title: Integrative metabolomics of cancer detection and progression; Protocol number: AN-5676; Expiration date: 01/19/2029).

Competing interests

Dr. Sreekumar reports grant from the Agilent Foundation, non-financial support from Sri Sathya Sai Institute for Higher Learning, India, and personal fees from Karkinos Health Care Pvt. Ltd., India, outside the submitted work. The remaining authors declare no competing interests.

Author details

[1]Department of Molecular and Cellular Biology, Baylor College of Medicine, Houston, Texas, United States
[2]Department of Radiation Oncology, University of Michigan, Ann Arbor, Michigan, United States
[3]Epidemiology and Population Science, Institute for Clinical and Translational Research, Baylor College of Medicine, Houston, Texas, United States
[4] Department of Molecular and Human Genetics, Baylor College of Medicine, Houston, Texas, United States
[5]Advanced Technology cores, Dan L Duncan Comprehensive Cancer Center, Baylor College of Medicine, Houston, Texas, United States
[6]Department of Pathology, Heersink School of Medicine, The University of Alabama at Birmingham, Birmingham, United States
[7]Michael E. DeBakey Veteran Affairs Medical Center, Houston, Texas, United States
[8]Department of Urology, Baylor College of Medicine, Houston, Texas, United States
[9]Dan L. Duncan Comprehensive Cancer Center, Baylor College of Medicine, Houston, Texas, United States
[10]Department of Pathology & Immunology, Baylor College of Medicine, Houston, Texas, United States

Received: 18 August 2025 / Accepted: 20 January 2026
Published online: 29 January 2026

References

1. Siegel RL, Miller KD, Wagle NS, Jemal A. Cancer statistics, 2023. CA Cancer J Clin. 2023;73(1):17–48.
2. Rebbeck TR. Prostate cancer disparities by race and ethnicity: from nucleotide to neighborhood. Cold Spring Harb Perspect Med. 2018;8(9):a030387.
3. Ravindran A, Krieger KL, Kaushik AK, Hovington H, Mehdi S, Piyarathna DWB, et al. Uridine diphosphate glucuronosyl transferase 2B28 (UGT2B28) promotes tumor progression and is elevated in African American prostate cancer patients. Cells. 2022;11(15):2329.
4. Krieger KL, Gohlke JH, Lee KJ, Piyarathna DWB, Castro PD, Jones JA, et al. Repair-Assisted damage detection reveals biological disparities in prostate cancer between African Americans and European Americans. Cancers. 2022;14(4):1012.
5. Gohlke JH, Lloyd SM, Basu S, Putluri V, Vareed SK, Rasaily U, et al. Methionine-Homocysteine pathway in African-American prostate cancer. JNCI Cancer Spectr. 2019;3(2):pkz019.
6. Ravindran A, Piyarathna DWB, Gohlke J, Putluri V, Soni T, Lloyd S, et al. Lipid alterations in African American men with prostate cancer. Metabolites. 2021;12(1):8.
7. Piyarathna DWB, Balasubramanian A, Arnold JM, Lloyd SM, Karanam B, Castro P, et al. ERR1- and PGC1α-associated mitochondrial alterations correlate with pan-cancer disparity in African Americans. J Clin Investig. 2019;129(6):2351–6.
8. Charles C, Lloyd SM, Piyarathna DWB, Gohlke J, Rasaily U, Putluri V, et al. Role of adenosine deaminase in prostate cancer progression. Am J Clin Exp Urol. 2023;11(6):594–612.
9. McHugh J, Saunders EJ, Dadaev T, McGrowder E, Bancroft E, Kote-Jarai Z, et al. Prostate cancer risk in men of differing genetic ancestry and approaches to disease screening and management in these groups. Br J Cancer. 2022;126(10):1366–73.
10. Powell IJ, Dyson G, Land S, Ruterbusch J, Bock CH, Lenk S, et al. Genes associated with prostate cancer are differentially expressed in African American and European American men. Cancer Epidemiol Biomarkers Prev. 2013;22(5):891–7.
11. Löffler M, Carrey EA, Knecht W. The pathway to pyrimidines: the essential focus on dihydroorotate dehydrogenase, the mitochondrial enzyme coupled to the respiratory chain. Nucleosides Nucleotides Nucleic Acids. 2020;39(10–12):1281–305.
12. Madak JT, Bankhead A, Cuthbertson CR, Showalter HD, Neamati N. Revisiting the role of dihydroorotate dehydrogenase as a therapeutic target for cancer. Pharmacol Ther. 2019;195:111–31.
13. Kayamori K, Nagai Y, Zhong C, Kaito S, Shinoda D, Koide S, et al. DHODH Inhibition synergizes with DNA-demethylating agents in the treatment of myelodysplastic syndromes. Blood Adv. 2021;5(2):438–50.
14. Sykes DB, Kfoury YS, Mercier FE, Wawer MJ, Law JM, Haynes MK, et al. Inhibition of dihydroorotate dehydrogenase overcomes differentiation Blockade in acute myeloid leukemia. Cell. 2016;167(1):171–e18615.
15. Guo S, Miao M, Wu Y, Pan D, Wu Q, Kang Z, et al. DHODH Inhibition represents a therapeutic strategy and improves abiraterone treatment in castration-resistant prostate cancer. Oncogene. 2024;43(19):1399–410.
16. The Cancer Genome Atlas Research Network, Weinstein JN, Collisson EA, Mills GB, Shaw KRM, Ozenberger BA, et al. The cancer genome atlas Pan-Cancer analysis project. Nat Genet. 2013;45(10):1113–20.
17. Ross-Adams H, Lamb AD, Dunning MJ, Halim S, Lindberg J, Massie CM, et al. Integration of copy number and transcriptomics provides risk stratification in prostate cancer: A discovery and validation cohort study. EBioMedicine. 2015;2(9):1133–44.
18. Wang Y, Xia XQ, Jia Z, Sawyers A, Yao H, Wang-Rodriquez J, et al. *Silico* estimates of tissue components in surgical samples based on expression profiling data. Cancer Res. 2010;70(16):6448–55.
19. Jia Z, Wang Y, Sawyers A, Yao H, Rahmatpanah F, Xia XQ, et al. Diagnosis of prostate cancer using differentially expressed genes in stroma. Cancer Res. 2011;71(7):2476–87.
20. Jain S, Lyons CA, Walker SM, McQuaid S, Hynes SO, Mitchell DM, et al. Validation of a metastatic assay using biopsies to improve risk stratification in patients with prostate cancer treated with radical radiation therapy. Ann Oncol. 2018;29(1):215–22.
21. Chen S, Zhu G, Yang Y, Wang F, Xiao YT, Zhang N, et al. Single-cell analysis reveals transcriptomic remodellings in distinct cell types that contribute to human prostate cancer progression. Nat Cell Biol. 2021;23(1):87–98.
22. Charles C, Gohlke J, Lloyd S, Henderson J, Karanam B, Navone N, et al. Metabolic rewiring in African-American prostate cancer: a role for adenosine-inosine axis in tumor progression. Cancer Epidemiol Biomarkers Prev. 2020;29(6Supplement2):A095–095.
23. Hooker SE, Woods-Burnham L, Bathina M, Lloyd S, Gorjala P, Mitra R, et al. Genetic ancestry analysis reveals misclassification of commonly used cancer cell lines. Cancer Epidemiol Biomarkers Prev. 2019;28(6):1003–9.
24. Frazier AE, Thorburn DR. Biochemical analyses of the electron transport chain complexes by spectrophotometry. In: Wong PD, LJC, editors. Mitochondrial disorders [Internet]. Methods in Molecular Biology. Volume 837. Totowa, NJ: Humana; 2012. pp. 49–62.
25. Ma Y, Bai RK, Trieu R, Wong LJC. Mitochondrial dysfunction in human breast cancer cells and their transmitochondrial cybrids. Biochimica et biophysica acta (BBA). - Bioenergetics. 2010;1797(1):29–37.
26. Parab AR, Salazar AM, Bark SJ, Divenko M, Putluri V, Lieu D, et al. A scalable organoid model of urothelial aging for metabolic interrogation, infection modeling, and reversal of age-associated changes. BioRxiv. 2025;2025.06.27.662009.

27. Lu Y, Pang Z, Xia J. Comprehensive investigation of pathway enrichment methods for functional interpretation of LC–MS global metabolomics data. Brief Bioinform. 2023;24(1):bbac553.
28. Krueger F, Andrews SR. Bismark: a flexible aligner and methylation caller for Bisulfite-Seq applications. Bioinf. 2011;27(11):1571–2.
29. Li H, Handsaker B, Wysoker A, Fennell T, Ruan J, Homer N, et al. The sequence Alignment/Map format and samtools. Bioinformatics. 2009;25(16):2078–9.
30. Park Y, Wu H. Differential methylation analysis for BS-seq data under general experimental design. Bioinformatics. 2016;32(10):1446–53.
31. Zhou Y, Tao L, Zhou X, Zuo Z, Gong J, Liu X, et al. DHODH and cancer: promising prospects to be explored. Cancer Metab. 2021;9(1):22.
32. Ashton NW, Jaiswal N, Moreno NC, Semenova IV, D'Orlando DA, Latancia MT, et al. A novel interaction between RAD23A/B and Y-family DNA polymerases. J Mol Biol. 2023;435(24):168353.
33. Lillard JW, Moses KA, Mahal BA, George DJ. Racial disparities in black men with prostate cancer: A literature review. Cancer. 2022;128(21):3787–95.
34. Park JW, Lee JK, Phillips JW, Huang P, Cheng D, Huang J, et al. Prostate epithelial cell of origin determines cancer differentiation state in an organoid transformation assay. Proc Natl Acad Sci USA. 2016;113(16):4482–7.
35. Kawatani M, Aono H, Hiranuma S, Shimizu T, Muroi M, Nogawa T, et al. Identification of a dihydroorotate dehydrogenase inhibitor that inhibits cancer cell growth by proteomic profiling. Oncol Res. 2023;31(6):833–44.
36. Teng D, Swanson KD, Wang R, Zhuang A, Wu H, Niu Z, et al. DHODH modulates immune evasion of cancer cells via CDP-Choline dependent regulation of phospholipid metabolism and ferroptosis. Nat Commun. 2025;16(1):3867.
37. Vikramdeo KS, Sharma A, Anand S, Sudan SK, Singh S, Singh AP, et al. Mitochondrial alterations in prostate cancer: roles in pathobiology and Racial disparities. IJMS. 2023;24(5):4482.
38. Yang H, Liu Y, Bai F, Zhang JY, Ma SH, Liu J, et al. Tumor development is associated with decrease of TET gene expression and 5-methylcytosine hydroxylation. Oncogene. 2013;32(5):663–9.
39. Ducker GS, Rabinowitz JD. One-Carbon metabolism in health and disease. Cell Metabol. 2017;25(1):27–42.
40. Camarena V, Sant DW, Huff TC, Mustafi S, Muir RK, Aron AT, et al. cAMP signaling regulates DNA hydroxymethylation by augmenting the intracellular labile ferrous iron pool. eLife. 2017;6:e29750.
41. Tsouko E, Khan AS, White MA, Han JJ, Shi Y, Merchant FA, et al. Regulation of the Pentose phosphate pathway by an androgen receptor–mTOR-mediated mechanism and its role in prostate cancer cell growth. Oncogenesis. 2014;3(5):e103–103.
42. Sakellakis M, Flores LJ. Androgen receptor signaling–mitochondrial DNA–oxidative phosphorylation: A critical triangle in early prostate cancer. Curr Urol. 2022;16(4):207–12.
43. Kamdar S, Isserlin R, Van Der Kwast T, Zlotta AR, Bader GD, Fleshner NE, et al. Exploring targets of TET2-mediated methylation reprogramming as potential discriminators of prostate cancer progression. Clin Epigenet. 2019;11(1):54.
44. Bedi U, Mishra VK, Wasilewski D, Scheel C, Johnsen SA. Epigenetic plasticity: A central regulator of epithelial-to-mesenchymal transition in cancer. Oncotarget. 2014;5(8):2016–29.
45. Holton NW, Ebenstein Y, Gassman NR. Broad spectrum detection of DNA damage by repair assisted damage detection (RADD). DNA Repair. 2018;66–67:42–9.

Publisher's note